HIGH-FIDELITY NUMERICAL MODELLING OF COLD SPATTER FORMATION DURING LASER POWDER BED FUSION OF 316-L STAINLESS STEEL

M. BAYAT*,[1], J. H. HATTEL*

*Technical University of Denmark (DTU), Building 425, Kgs. 2800 Lyngby, Denmark
[1]Corresponding author

DOI 10.3217/978-3-85125-968-1-01

ABSTRACT

Spatter and denudation are two very well-known phenomena occurring mainly during the laser powder bed fusion process and are defined as ejection and displacement of powder particles, respectively. The main driver of this phenomenon is the formation of a vapor plume jet that is caused by the vaporization of the melt pool which is subjected to the laser beam. In this work, a 3-dimensional transient turbulent computational fluid dynamics model coupled with a discrete element model is developed in the finite volume-based commercial software package Flow-3D AM to simulate the spatter phenomenon. The numerical results show that a localized low-pressure zone forms at the bottom side of the plume jet and this leads to a pseudo-Bernoulli effect that drags nearby powder particles into the area of influence of the vapor plume jet. As a result, the vapor plume acts like a momentum sink and therefore all nearby particles point are dragged towards this region. Furthermore, it is noted that due to the jet's attenuation, powder particles start diverging from the central core region of the vapor plume as they move vertically upwards. It is moreover observed that only particles which are in the very central core region of the plume jet get sufficiently accelerated to depart the computational domain, while the rest of the dragged particles, especially those which undergo an early divergence from the jet axis, get stalled pretty fast as they come in contact with the resting fluid. In the last part of the work, two simulations with two different scanning speeds are carried out, where it is clearly observed that the angle between the departing powder particles and the vertical axis of the plume jet increases with increasing scanning speed.

Keywords: Spatter, Denudation, Discrete Element Method, Computational Fluid Dynamics, L-PBF, Additive Manufacturing

INTRODUCION

Metal additive manufacturing (MAM) processes are capable of manufacturing very complex metallic components, which are near-to-impossible to make via the current existing conventional processes such as milling and casting. MAM are broadly classified into three primary groups of directed energy deposition (DED), powder bed fusion (PBF) and sheet lamination processes, according to the ASTM standard [1]. Nevertheless, DED

and PBF have received much more attention from both industrial sectors and academia thanks to DED and PBF's high degree of freedom and at the same time their inherent complexity, respectively.

One of the main issues of MAM processes (since we will only focus on DED and PBF, we will use the term MAM to refer to these two processes, henceforth, we will use MAM) is their complexity which is mainly due to the coexistence of a plethora of dependent interactive physical phenomena. These physical phenomena cover a long list ranging from melting, solidification, evaporation, ablation, laser-material interaction, absorption, the Marangoni effect, capillarity and evaporative recoil pressure occurring at meso-scale [2] to micro-scale phenomena such as dendrites' growth and nucleation, epitaxial grain growth and solid state phase transformation [3], [4]. Furthermore, all these physical phenomena occur within a very short timeframe in the order of sub-milliseconds [5] and therefore MAM processes, especially the PBF processes, are highly prone to instabilities. Therefore, any inaccurate selection of input process parameters could potentially lead to defects in the final components and such defects could simply disqualify the sample for the end users.

Over the past few years, advanced numerical simulations have been increasingly used to determine a process window comprising selected input process parameters with two ultimate goals of obtaining a defect-free component and unraveling defect formation mechanisms [6]–[8]. These models could be categorized based on several criteria such as length-scale [9], fidelity level and the involved physics [10] and type of coupling between these physics [11].

One of the two most complicated physical phenomena in PBF (mostly in LPBF) processes are spattering and denudation which are defined as the ejection of powder particles near to the melt pool and then their follow-up unwanted displacement in the vicinity of the scan tracks [12]. Compared to the colossal amount of research contributions that are dedicated to conduction- or transport-based melt pool simulations, there have been perhaps less than a dozen papers on the modelling of spatter and denudation [13]. Masmoudi, Bolot and Coddet. [14] attempted to simulate the vapor plume formation (the main driver of the spatter and denudation phenomena) via adding a mass source term in their model. Bidare et al. [15] made a somewhat more advanced finite element-based 2-dimensional model by taking the thermal aspects of the LPBF process, namely the laser heating effect via a Gaussian heat flux, into consideration and they found the vapour jet's velocity magnitude based on the Knudsen layer's approach. Recently, Bitharas et al. [16] extended this model to 3 dimensions. However, in the same manner as both the two earlier-mentioned works [14], [15], powder particles were not explicitly modelled in these simulations. Li and Tan [17], [18] developed a more advanced model and besides simulating the vapor plume via a continuum-based approach, they modelled particles' motion via the Lagrangian particle tracking method. Nevertheless, they only simulated a limited spatial domain with few powder particles under 2D axisymmetric assumptions.

In this work, we aim to understand the underlying mechanisms behind the spatter phenomenon and its relationship with the denudation of the powder layer via advanced numerical simulation. Therefore, we have developed a coupled finite volume (FVM)-based computational fluid dynamics (CFD) model coupled with the discrete element method (DEM) in the commercial software package Flow-3D, using the AM module. The

CFD model solves coupled partial differential equations of continuity, Raynolds Average Navier-Stokes (RANS), conservation of kinetic energy, conservation of dissipation of kinetic energy and finally, heat transfer. The DEM model solves equations of motions as well as the energy balance equation, based on a lumped thermal body assumption, for every individual powder particle while taking the interaction of powder particles and their collision into account. In the following section, we will go through the modelling details and assumptions for the CFD-DEM model and then we will explain and discuss the results and we will show how different choices of input process parameters can affect the powder dynamics in LPBF.

NUMERICAL MODEL

In this section, first, we will go through fluid and particles' motion and heat transfer equations and then we will describe the details of the computational domain and the added boundary conditions.

GOVERNING PHYSICS: FLUID AND PARTICLE MOTION

Fluid flow motion

The coupled partial differential equations (PDE) of continuity, time-averaged Navier-Stokes, , conservation of kinetic energy and finally, conservation of dissipation of kinetic energy are jointly solved to find the pressure and velocity field vectors in the computational domain belonging to the gas phase. Continuity and the Navier-Stokes equations are given below [19]

$$\frac{\partial u_i^F}{\partial x_i} = 0, \tag{1}$$

$$\rho\left[\frac{\partial}{\partial t}u_i^F + \frac{\partial}{\partial x_j}(u_j^F u_i^F)\right] = -\frac{\partial p}{\partial x_i} + \rho g_i + \frac{\partial}{\partial x_j}\left(\sigma_{ij} + \tau_{ij}\right) + \Phi_i, \tag{2}$$

and u_i^F (m.s^{-1}) is the fluid velocity vector and ρ (kg.m^{-3}) is fluid's density and the two last terms inside the divergent operator, σ_{ij} (Pa) and τ_{ij} (Pa) are viscous and turbulent stress tensors and the last term in equation (2) is the source term expressing external volumetric forces. However, in this work it is assumed that the sum of forces exerted on the fluid domain by the moving powder particles is negligible.

$$\sigma_{ij} = \mu_f\left(\frac{\partial u_i^F}{\partial x_j} + \frac{\partial u_j^F}{\partial x_i}\right), \tag{3}$$

$$\tau_{ij} = \mu_{turb}\left(\frac{\partial u_i^F}{\partial x_j} + \frac{\partial u_j^F}{\partial x_i}\right) - \frac{2}{3}\rho k\delta_{ij}, \tag{4}$$

$$\mu_{turb} = \rho C_\mu \frac{k^2}{\varepsilon}, \tag{5}$$

where μ_f (Pa.s) and μ_{turb} (Pa.s) are fluid and turbulent viscosity, respectively [20]–[22]. k ($m^2.s^{-2}$) is the turbulent kinetic energy per unit mass for the host fluid, expressed in equations (4) and (5) and ε ($m^2.s^{-3}$) is the dissipation rate of k ($m^2.s^{-2}$).

$$\rho\left[\frac{\partial}{\partial t}k+\frac{\partial}{\partial x_j}(u_j^F k)\right]=\frac{\partial}{\partial x_j}\left[\left(\mu_f+\frac{\mu_{turb}}{\sigma_k}\right)\frac{\partial k}{\partial x_j}\right]+\Pi-\rho\varepsilon \tag{6}$$

$$\rho\left[\frac{\partial}{\partial t}\varepsilon+\frac{\partial}{\partial x_j}(u_j^F \varepsilon)\right]=\frac{\partial}{\partial x_j}\left[\left(\mu_f+\frac{\mu_{turb}}{\sigma_\varepsilon}\right)\frac{\partial \varepsilon}{\partial x_j}\right]+\frac{\varepsilon}{k}(C_{\varepsilon 1}\Pi-\rho\varepsilon C_{\varepsilon 2}), \tag{7}$$

$$\Pi=\tau_{ij}\frac{\partial u_i^F}{\partial x_j}. \tag{8}$$

Equations (6) and (7) are transient PDEs of conservation of turbulent kinetic energy and rate of change of turbulent kinetic energy, respectively.

Particles' motion dynamics

The transient motion of the powder particles is described in the Lagrangian framework and found via solving the following particle force balance equation using DEM [23]

$$m_p\frac{d^2X_i}{dt^2}=6\pi\mu_f R_p\left(u_i^F-U_i^p\right)+F_i^{collision}+m_p\left(1-\frac{\rho_F}{\rho_p}\right). \tag{9}$$

R (m) and m_p (kg) are spherical particle's radius and mass, respectively. X_i (m) and U_i ($m.s^{-1}$) are displacement and velocity vector of particles, in equation (9). The first term on the right hand side of equation (9) is related to viscous drag forces due to the particle-fluid interaction and the second term expresses forces due to particles' collisions, while the last term is related to the combined buoyancy-gravity effect.

$$F_i^{collision}=\left(\sum k_{eff}X_i^{rel}+\sum \eta_{eff}U_i^{rel}\right) \tag{10}$$

k_{eff} ($N.m^{-1}$) and η_{eff} ($N.m^{-1}.s^{-1}$) are effective spring and damping coefficients and superscript $(.)^{rel}$ stands for relative motion. And finally and after all the fluid-induced as well as collision forces are calculated, the location of every individual powder particle is determined via

$$\frac{dX_i^p}{dt}=U_i^p \tag{11}$$

GOVERNING PHYSICS: HEAT TRANSFER

The host fluid and powder particles transfer heat to each other and their temperature gets updated after every increment. Transient PDE of heat transfer in 3 dimensions is solved in the hosting fluid domain to find the temperature field for the chamber gas, whereas transient zero dimension heat balance, derived based on the lumped thermal assumption, is solved for every individual powder particle to find their temperature. Contrary to the one-way coupling between the fluid flow motion and particle dynamics, where fluid-

induced viscous drag forces are added on powder particles, two-way thermal coupling is implemented in this paper, and this takes place via convection heat transfer.

Fluid heat transfer

The transient temperature field in the fluid domain is determined by solving PDE of heat balance in the host fluid domain

$$\rho c_p \left[\frac{\partial T}{\partial t} + \frac{\partial}{\partial x_j}(u_j^F T)\right] = \frac{\partial}{\partial x_j}\left(k\frac{\partial T}{\partial x_j}\right) + \frac{\sum h_{P-F} A_{eff}(T_p - T)}{\forall_c}, \quad (12)$$

where c_p (J.kg^{-1}.K^{-1}) and k (W.m^{-1}.K^{-1}) are specific heat capacity and thermal conductivity of the fluid in equation (12). The last term in equation (12) is volumetric heat source due to heat transfer from powder particles to the fluid domain within a cell volume V_c and $h_{P\text{-}F}$ (W.m^{-2}.K^{-1}) is the convective heat transfer coefficient which is determined by [24]

$$Nu = \frac{2h_{P-F}R}{k} = 2 + 0.6Re^{0.5}Pr^{0.33}. \quad (13)$$

Re (-) and *Pr* (-) are Reynolds and Prandtl numbers in equation (13).

Particles heat transfer

The transient temperature of individual powder particles are found via the following equation [25], [26]

$$m_p c_p^p \frac{dT_p}{dt} = h_{P-F} A_{eff}(T - T_P), \quad (14)$$

and $c^p{}_p$ (J.kg^{-1}.K^{-1}) is the specific heat capacity of powder particles. Moreover, in this work the radiation heat transfer is ignored since it is believed that convection is the main mechanism of heat transfer to the particles due to the very high velocity magnitude of the vapor jet plume.

COMPUTATIONAL DOMAIN AND BOUNDARY CONDITIONS

Fig. 1 shows a front and a side view of the fluid domain. The impact of the vapor plume is modelled with a moving momentum source with an upward velocity of 100 m.s^{-1} which is an average of the previous experimental observations [27], [28]. Furthermore, the momentum source has a fixed temperature of 3000 K, which is close to the boiling temperature of 316-L stainless steel. For such explicit representation of the evaporation plume, it is not possible to involve certain input process parameters such as laser power and the beam size, as the thermal impact from the laser beam is already taken into account by the initial temperature of the jet.

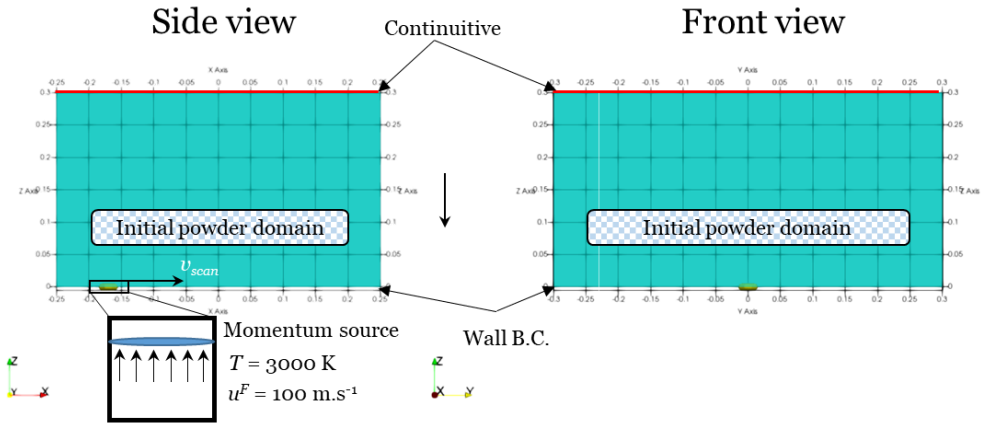

Fig. 1 Two different views of the computational domain for the fluid domain. The vapor plume is simulated by a moving momentum source with a prescribed temperature of 3000 K.

The overall size of the computational domain as also shown in Fig. 1 is 5.00 mm by 6.00 mm by 3.00 mm and the CFD cell size is set to 45 µm and this leads to 989121 cells with an aspect ratio of very close to unity. According to Fig. 1, powder particles are initially set inside the fluid domain at a certain distance from the bottom wall boundary condition. In total 15000 powder particles with four different sizes of 20 µm, 29 µm, 30 µm and 35 µm are set inside the fluid domain. The top boundary condition is set to continuative and this allows both the host fluid and particles to exit the domain. The rest of the boundary conditions are set to symmetry and this is valid as long as the region of interest where high velocity gradients occur, is at a relatively far distance from these boundaries. Details of the employed thermo-physical properties and the implemented process inputs are listed in Table 1.

Table 1 List of a number of input parameters and thermo-physical properties.

Property	Unit	Value	Property	Unit	Value
ρ_{air}	Kg.m^{-3}	1.225	$c_{p,air}$	J.kg^{-1}.K^{-1}	718
ρ_{steel}	Kg.m^{-3}	7900	$c_{p,steel}$	J.kg^{-1}.K^{-1}	804
k_{air}	W.m^{-1}.K^{-1}	2.346E-02	μ_{air}	Pa.s^{-1}	1.78E-05
k_{steel}	W.m^{-1}.K^{-1}	28	Jet speed	m.s^{-1}	100
v_{scan}	m.s^{-1}	0.3, 0.5	Jet diameter	m	2.00E-04

RESULTS AND DISCUSSION

Fig. 2 (a) and (b) show two snapshots from the top view of the powder layer morphology right before the scanning step and at 0.008 seconds during the scanning step, respectively. One can notice in Fig. (b) that the initial local powder layer arrangement is disrupted due to the fluid dynamics impact of the moving vapor plume.

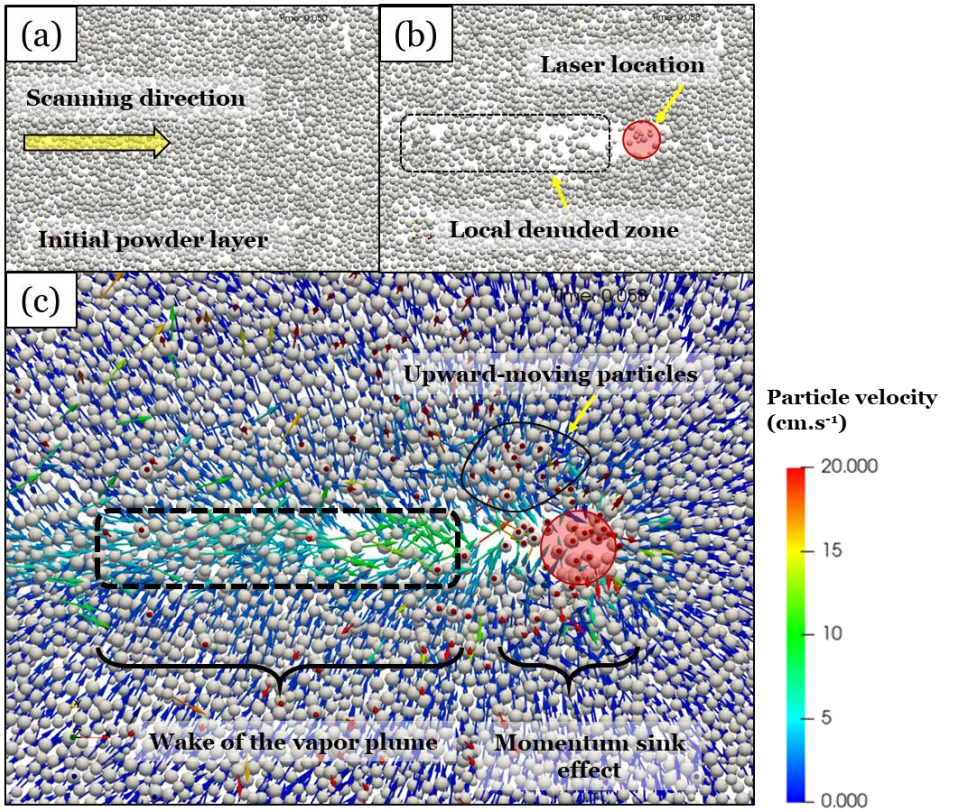

Fig. 2 (a) and (b) are two snapshots taken at an x-y plane parallel to the powder layer plane before and 0.008 seconds after the start of the scanning process. (c) Shows a magnified view of (b) where detailed powder particles' movement along with their velocity magnitude and directions are shown.

It is furthermore observed in both Fig. 2 (b) that a small region in the immediate wake of the vapor plume and on the powder layer, is striped of powder particles. This is because a noticeable fraction of the powder particles adjacent to the vapor plume's track, is pulled outwards along the z axis and as a result of the viscous drag force imposed by the high-velocity upward plume in those regions, see Fig. 2 (c). One can also clearly see in Fig. 2 (c) that a portion of particles possess vertically-upward velocities and this in essence creates a localized low-pressure region that to some extent and by some simplifying assumptions, is formed due to the Bernoulli effect. This pseudo-Bernoulli effect in turn, acts like a momentum sink in the local areas in the vicinity of the vapor plume. This could be better understood as, according to Fig. 2 (c), all the nearby powder particles are pointing towards this momentum sink area.

Fig. 3 shows the particles' temperature contour as well as their instantaneous trajectories colored with particles' velocity magnitude from the front view.

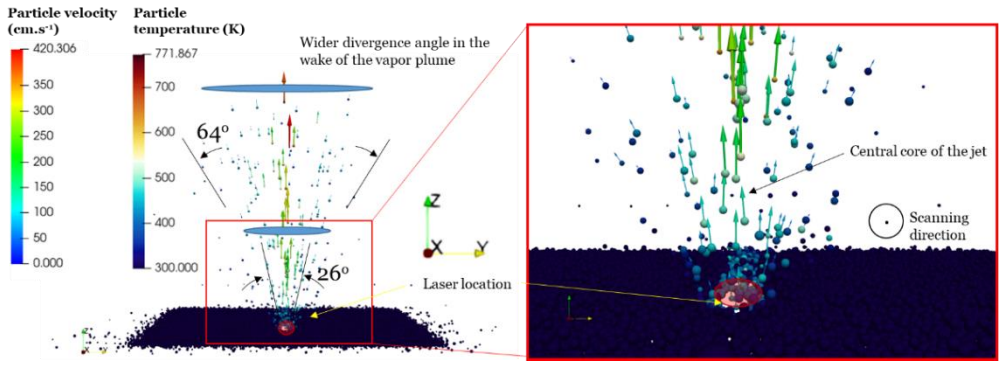

Fig. 3 Front view of the ejected powder particles due to the plume movement. Powder particles are colored by their respective temperature while trajectory colors show their magnitude at 0.007 seconds.

Based on Fig. 3 it is noted that although the vapor plume is vertically upwards, powder particles which are impacted by this jet, eject at an angle of approximately 26 degrees right in the zone where the vapor plume is active. At the same time, it is also observed in Fig. 3 that particles' divergence angle increases with an increase in their distance from the plume. This could be attributed to the jet attenuation that typically occurs when a jet is ejected into the nearby resting fluid. To better clarify this growing divergence of the escaping powder particles, contours of the velocity magnitude of the vapor jet and at two vertical locations of 200 μm and 2000 μm from the powder bed are shown in Fig. 4 (b). According to this figure, it is noted that due to the impact of the neighboring static fluid on the vapor plume, the jet's maximum velocity magnitude is decreased while at the same time, its area of influence is widened, underlining the jet's momentum attenuation. Therefore, the powder particles that are directly impacted by the vapor plume, obtain dominantly-vertical but diverging velocities and this leads to their divergence from the vertical direction. Interestingly, it is furthermore noted that those particles which are in line with the central core region of the jet, keep their vertical velocity since there is no noticeable radial velocity at this very core region.

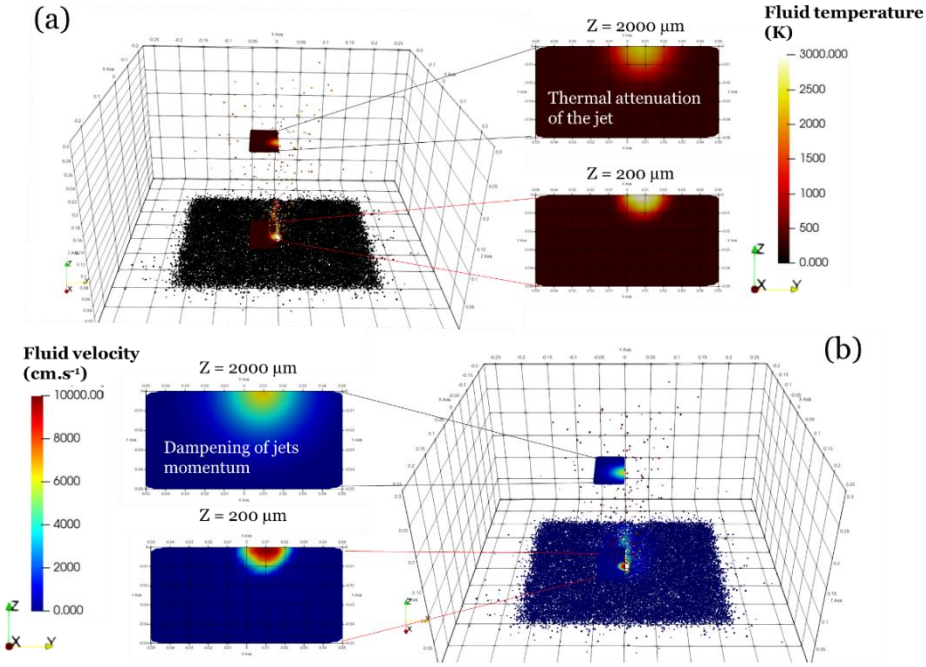

Fig. 4 (a) Temperature contour of powder particles along with contours of vapor plumes temperature at two vertical distances of 200 µm and 2000 µm from the powder bed. (b) 3D velocity magnitude contours of powder particles and 2D velocity contour of the jet at 200 µm and 2000 µm from the powder bed.

The powder particles also transfer heat with the fluid and according to Fig. 3, it is noticed that the maximum powder particles temperature rises to about 772 K. This temperature rise is a result of strong convection between the jet and particles. According to the blow-up part of Fig. 3, only a narrow region of the powder bed undergoes an observable temperature change and this is ascribed to the low thermal conductivity of the powder bed, which is in essence caused by imperfect point contacts with high thermal resistance between particles. Moreover, in the same manner as observed before, the maximum temperature of the plume also declines as the jet moves further inside the nearby resting fluid.

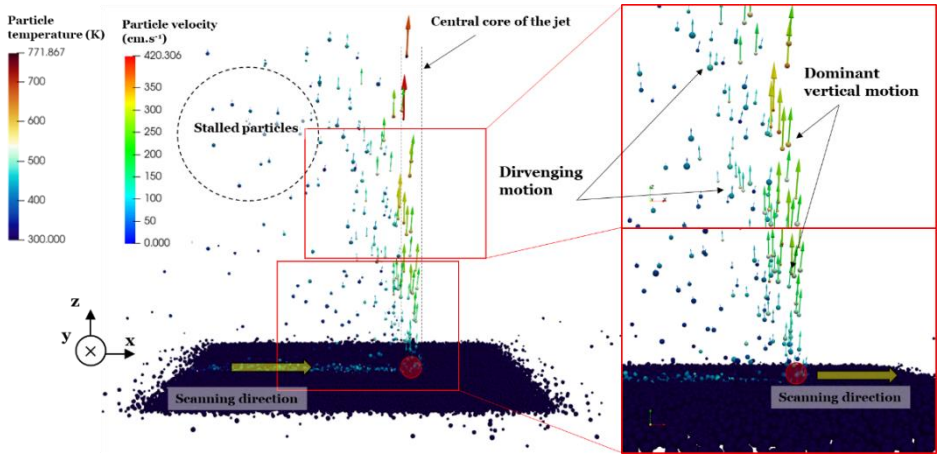

Fig. 5 Side view of the departing particle - particles are colored with their temperature and particle velocities are colored with particles' velocity magnitude.

Fig. 5 demonstrates a side view of the spattering effect and it is clearly seen in this figure that those particles which move inside the central core of the plume's jet, are accelerated to a maximum velocity of 4.2 $m.s^{-1,}$ which is primarily vertical. When the plume moves along the scanning direction, those particles which were initially inside the core region, gradually lose their velocity due to the damping effect of the drag force of the resting fluid. One can see that at a distance of about 2 mm behind the central core of the jet, powder particles are stalled and undergo the so-called entrainment effect.

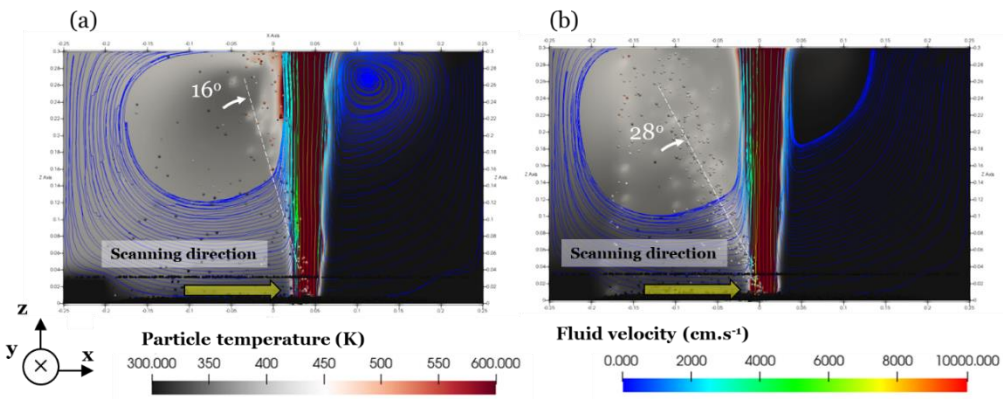

Fig. 6 Contours of fluid and particles temperature along with fluid's streamlines colored with velocity magnitude at (a) 300 $mm.s^{-1}$ and (b) 500 $mm.s^{-1}$

Fig. 6 (a) and (b) show contours of fluid and particle temperature from the side view for scanning speed of 300 $mm.s^{-1}$ and 500 $mm.s^{-1}$, respectively. The lines in this figure are streamlines that are colored with fluid's velocity magnitude. Based on Fig. 6, it is clearly noted that particles are ejected at an angle from the zone where the plume is formed. This angle is about 16° for a lower scanning speed of 300 $mm.s^{-1}$ and 28° for 500 $mm.s^{-1}$

scanning speed. The main reason behind this change of ejection angle with respect to the vertical plume jet is, as mentioned earlier, the fact that particles which are inside the central core of the jet, move almost vertically upwards. Therefore, the faster the translational speed of the plume, the shorter will be the vertical thrust of the powder particles. A very similar trend has also been observed in the *in-situ* online monitoring of the L-PBF process of 1.4404 stainless steel in [29] where it is shown that by increasing the scanning velocity of the laser beam, the jet angle deviates further from the perpendicular line normal to the build table. In this scenario, fewer particles will possess high vertical velocities at higher translational speed of the plume. To better understand this effect, one can go to the extreme case and imagine a static plume where the particles will move primarily parallel to the jet direction, thus, there will be no deviation between the jet and the ejected particles.

Furthermore, one can see in Fig. (a) and (b) how high-temperature powder particles that enter the fluid region behind the jet, locally affect the temperature field in the wake of the plume. Moreover, since the interaction time between particles and the jet is shorter at higher scanning speed, particles will have lower temperatures at higher scanning speeds.

CONCLUSION

In this work, a coupled particle-fluid dynamics numerical simulation of the L-PBF process is developed to study the spatter phenomenon and its resulting denudation. The model is developed in the commercial software package Flow-3D using its AM module and is made of two parts, a CFD model that simulates the heat and fluid flow conditions of the fluid phase, and a DEM model that predicts particles' motion dynamics as well as their thermal conditions. The modelling results demonstrate that the fluid dynamics impact of the high-velocity vapor plume jet creates a localized low-pressure zone near the plume location and this leads to a pseudo-Bernoulli effect that drags nearby powder particles inside the jet plume and then these particles will be lifted upwards due to the very high viscous drag force from the high-speed jet. As a result of this, a local denuded zone will form in the wake of the plume location. Furthermore, it is noted that the linear momentum of the jet starts becoming dampened as the jet comes into contact with neighboring static air. This will then lead to a diverging flow and as a result, powder particles also diverge from the central core of the vapor plume. These particles then quickly lose both their temperature and velocity as they get in contact with the resting static air. Moreover, two cases with scanning speeds of 300 $mm.s^{-1}$ and 500 $mm.s^{-1}$ were simulated and it is observed that the angle between ejecting powder particles and the vertical plume jet increases from 16^{o} to 28^{o}, mainly because in the latter case, particles have shorter contact with the jet and therefore have lower acceleration compared to the ejecting particles in the case with 300 $mm.s^{-1}$.

APPENDICES AND ACKNOWLEDGEMENTS

This work has received funding from Independent Research Fund Denmark, DIGI-3D project.

References

[1] T. DEBROY et al.: 'Additive manufacturing of metallic components – Process, structure and properties', *Prog Mater Sci*, vol. 92, pp. 112-224, 2018, doi: 10.1016/j.pmatsci.2017.10.001.

[2] M. MARKL and C. KÖRNER: 'Multiscale Modeling of Powder Bed–Based Additive Manufacturing', *Annu Rev Mater Res*, vol. 46, no. 1, pp. 93-123, 2016, doi: 10.1146/annurev-matsci-070115-032158.

[3] A. ZINOVIEV, O. ZINOVIEVA, V. PLOSHIKHIN, V. ROMANOVA and R. BALOKHONOV: 'Evolution of grain structure during laser additive manufacturing. Simulation by a cellular automata method', *Mater Des*, vol. 106, pp. 321-329, 2016, doi: 10.1016/j.matdes.2016.05.125.

[4] Y. ZHANG and J. ZHANG: 'Modeling of solidification microstructure evolution in laser powder bed fusion fabricated 316L stainless steel using combined computational fluid dynamics and cellular automata', *Addit Manuf*, vol. 28, no. July 2018, pp. 750-765, 2019, doi: 10.1016/j.addma.2019.06.024.

[5] A. A. MARTIN et al.: 'Ultrafast dynamics of laser-metal interactions in additive manufacturing alloys captured by in situ X-ray imaging', *Mater Today Adv*, vol. 1, p. 100002, 2019, doi: 10.1016/j.mtadv.2019.01.001.

[6] Y. C. WU et al.: 'Numerical modeling of melt-pool behavior in selective laser melting with random powder distribution and experimental validation', *J Mater Process Technol*, vol. 254, no. July 2017, pp. 72-78, 2018, doi: 10.1016/j.jmatprotec.2017.11.032.

[7] W. GAO, S. ZHAO, Y. WANG, Z. ZHANG, F. LIU and X. LIN: 'Numerical simulation of thermal field and Fe-based coating doped Ti', *Int J Heat Mass Transf*, vol. 92, pp. 83-90, 2016, doi: 10.1016/j.ijheatmasstransfer.2015.08.082.

[8] A. CHARLES, M. BAYAT, A. ELKASEER, L. THIJS, J. H. HATTEL and S. SCHOLZ: 'Elucidation of dross formation in laser powder bed fusion at down-facing surfaces: Phenomenon-oriented multiphysics simulation and experimental validation', *Addit Manuf*, vol. 50, 2022, doi: 10.1016/j.addma.2021.102551.

[9] C. MEIER, R. W. PENNY, Y. ZOU, J. S. GIBBS and A. J. HART: 'Thermophysical phenomena in metal additive manufacturing by selective laser melting: Fundamentals, modeling, simulation and experimentation', *ArXiv*, 2017, doi: 10.1615/annualrevheattransfer.2018019042.

[10] W. KING, A. T. ANDERSON, R. M. FERENCZ, N. E. HODGE, C. KAMATH and S. A. KHAIRALLAH: 'Overview of modelling and simulation of metal powder bed fusion process at Lawrence Livermore National Laboratory', *Materials Science and Technology* (United Kingdom), vol. 31, no. 8, pp. 957-968, 2015, doi: 10.1179/1743284714Y.0000000728.

[11] M. BAYAT, W. DONG, J. THORBORG, A. C. TO and J. H. HATTEL: 'A review of multi-scale and multi-physics simulations of metal additive manufacturing processes with focus on modeling strategies', *Addit Manuf*, vol. 47, 2021, doi: 10.1016/j.addma.2021.102278.

[12] M. J. MATTHEWS, G. GUSS, S. A. KHAIRALLAH, A. M. RUBENCHIK, P. J. DEPOND and W. E. KING: 'Denudation of metal powder layers in laser powder bed fusion processes', *Acta Mater*, vol. 114, pp. 33-42, 2016, doi: 10.1016/j.actamat.2016.05.017.

[13] H. CHEN and W. YAN: 'Spattering and denudation in laser powder bed fusion process: Multiphase flow modelling', *Acta Mater*, vol. 196, pp. 154-167, 2020, doi: 10.1016/j.actamat.2020.06.033.

[14] A. MASMOUDI, R. BOLOT and C. CODDET: 'Investigation of the laser-powder-atmosphere interaction zone during the selective laser melting process', *J Mater Process Technol*, vol. 225, pp. 122-132, 2015, doi: 10.1016/j.jmatprotec.2015.05.008.

[15] P. BIDARE, I. BITHARAS, R. M. WARD, M. M. ATTALLAH and A. J. MOORE: 'Fluid and particle dynamics in laser powder bed fusion', *Acta Mater*, vol. 142, pp. 107-120, 2018, doi: 10.1016/j.actamat.2017.09.051.

[16] I. BITHARAS, A. BURTON, A. J. ROSS and A. J. MOORE: 'Visualisation and numerical analysis of laser powder bed fusion under cross-flow', *Addit Manuf*, vol. 37, no. June 2020, p. 101690, 2021, doi: 10.1016/j.addma.2020.101690.

[17] X. LI and W. TAN: 'Numerical Modeling of Powder Gas Interaction Relative to Laser Powder Bed Fusion Process', *Journal of Manufacturing Science and Engineering*, vol. 143, no. May, pp. 1-7, 2021, doi: 10.1115/1.4048443.

[18] X. LI, C. ZHAO, T. SUN and W. TAN: 'Revealing transient powder-gas interaction in laser powder bed fusion process through multi-physics modeling and high-speed synchrotron x-ray imaging', *Addit Manuf*, vol. 35, no. June, p. 101362, 2020, doi: 10.1016/j.addma.2020.101362.

[19] H. M. DEYLAMI, N. AMANIFARD, S. S. HOSSEININEZHAD and F. DOLATI: 'Numerical investigation of the wake flow control past a circular cylinder with Electrohydrodynamic actuator', *European Journal of Mechanics*, B/Fluids, vol. 66, pp. 71-80, 2017, doi: 10.1016/j.euromechflu.2017.06.002.

[20] O. A. MARZOUK and E. DAVID HUCKABY: 'Simulation of a swirling gas-particle flow using different k-epsilon models and particle-parcel relationships', *Engineering Letters*, vol. 18, no. 1, 2010.

[21] B. AKAY, D. RAGNI, C. S. FERREIRA and G. J. W. VAN BUSSEL: 'Investigation of the root flow in a Horizontal Axis', *Wind Energy*, no. August 2016, pp. 1-20, 2013, doi: 10.1002/we.

[22] A. J. LEW, G. C. BUSCAGLIA and P. M. CARRICA: 'A Note on the Numerical Treatment of the k-epsilon Turbulence Model', *Int J Comut Fluid Dyn*, vol. 14, no. 3, pp. 201-209, 2001, doi: 10.1080/10618560108940724.

[23] A. AGGARWAL et al.: 'Role of impinging powder particles on melt pool hydrodynamics, thermal behaviour and microstructure in laser-assisted DED process: A particle-scale DEM – CFD – CA approach', *Int J Heat Mass Transf*, vol. 158, p. 119989, 2020, doi: 10.1016/j.ijheatmasstransfer.2020.119989.

[24] X. GUAN and Y. F. ZHAO: 'Numerical modeling of coaxial powder stream in laser-powder-based Directed Energy Deposition process', *Addit Manuf*, vol. 34, no. April, p. 101226, 2020, doi: 10.1016/j.addma.2020.101226.

[25] S. Y. WEN, Y. C. SHIN, J. Y. MURTHY and P. E. SOJKA: 'Modeling of coaxial powder flow for the laser direct deposition process', *Int J Heat Mass Transf*, vol. 52, no. 25-26, pp. 5867-5877, 2009, doi: 10.1016/j.ijheatmasstransfer.2009.07.018.

[26] M. BAYAT et al.: 'On the role of the powder stream on the heat and fluid flow conditions during Directed Energy Deposition of maraging steel – Multiphysics

modeling and experimental validation', *Addit Manuf*, vol. 43, 2021, doi: 10.1016/j.addma.2021.102021.

[27] P. BIDARE, I. BITHARAS, R. M. WARD, M. M. ATTALLAH and A. J. MOORE: 'Laser powder bed fusion in high-pressure atmospheres', *International Journal of Advanced Manufacturing Technology*, vol. 99, no. 1-4, pp. 543-555, 2018, doi: 10.1007/s00170-018-2495-7.

[28] P. BIDARE, I. BITHARAS, R. M. WARD, M. M. ATTALLAH and A. J. MOORE: 'Fluid and particle dynamics in laser powder bed fusion', *Acta Mater*, vol. 142, pp. 107-120, 2018, doi: 10.1016/j.actamat.2017.09.051.

[29] E. ESCHNER, T. STAUDT and M. SCHMIDT: 'Sensing approach for the in-situ determination of spatter motion within PBF-LB/M', *CIRP Annals*, vol. 71, no. 1, pp. 149-152, Jan. 2022, doi: 10.1016/j.cirp.2022.03.005.